JOURNAL OF COMPUTATIONAL PHYSICS 104, 361–376 (1993)

# An Adaptive Lagrangian Method for Computing 1D Reacting and Non-reacting Flows

TASSO LAPPAS, ANTHONY LEONARD, AND PAUL E. DIMOTAKIS

*Graduate Aeronautical Laboratories, California Institute of Technology, Pasadena, California 91125*

Received April 5, 1991; revised April 20, 1992

A method for computing one-dimensional unsteady compressible flows, with and without chemical reactions is presented. This work has focused on the accurate computation of the discontinuous waves that arise in such flows. The main feature of the method is the use of an adaptive Lagrangian grid. This allows the computation of discontinuous waves and their interactions with the accuracy of front-tracking algorithms. This is done without the use of additional grid points representing shocks, in contrast to conventional front-tracking schemes. The Lagrangian character of the present scheme also allows contact discontinuities to be captured easily. The algorithm avoids interpolation across discontinuities in a natural and efficient way. The method has been used on a variety of reacting and non-reacting flows in order to test its ability to compute accurately and in a robust way complicated wave interactions. © 1993 Academic Press, Inc.

## 1. INTRODUCTION

Several methods for computing unsteady inviscid compressible flows have appeared in the literature in recent years. The emphasis has been on the ability of these numerical schemes to compute accurately discontinuous waves which develop and their interactions.

High-resolution shock-capturing methods for hyperbolic conservation laws is one category of such methods which have been used successfully in recent years. A basic feature of these methods is that the conservative formulation is used which allows for shocks and their interactions to be captured automatically without special effort. This is characteristic of all older shock-capturing methods, such as the Lax–Wendroff scheme [8], the MacCormack scheme [10], the original Godunov scheme [5]. In all such methods, discontinuous waves of the solution are represented as steep fronts, i.e., smeared over a finite number of computational cells. A second and more important feature of recent high-resolution schemes is the special effort which is made to achieve higher order spatial and temporal accuracy so as to represent discontinuous waves of the solution as accurately as possible, i.e., to reduce the smearing effect which is typical of all shock-capturing methods. Such schemes are the TVD schemes [6, 7], the various MUSCL-type schemes [15], the PPM scheme [3] (piecewise parabolic method), etc. A comparative study of some of these schemes for real gases is given in a review article by Montagné *et al.* [11]. The basic high-resolution shock-capturing methods have been developed for nonlinear scalar hyperbolic conservation laws. It is for this case that there exists a sound mathematical theory. For nonlinear hyperbolic systems of equations in one space variable the theory is not as clear and the numerical methods used for these systems apply formally the same techniques as in the scalar case, but with the additional use of exact or approximate Riemann solvers. A classical Riemann problem is solved locally at each computational cell boundary in order to compute the various flux terms required. This is the essential ingredient of the original Godunov scheme and it is present in most successful high-resolution schemes. The various flux-vector splitting techniques [14, 16] have essentially incorporated in them an approximate Riemann solver. Finally, their extension to more than one space dimension is usually done by treating each spatial dimension separately.

Another category of numerical schemes that have been used is that of the shock-fitting or front-tracking methods. Although they have not been used as extensively as the shock-capturing methods, they have been quite successful in one-dimensional problems. A good review of these methods, as well as of many shock capturing methods, is given by Moretti [12]. These schemes are typically based on a non-conservative formulation and an effort is made to detect and identify the various discontinuous waves and compute their interactions explicitly. This is usually accomplished by introducing additional computational elements representing such waves and using the Rankine–Hugoniot jump conditions. This technique leads to complex programming logic. Identifying the waves and computing their interactions accurately is crucial for obtaining a meaningful and stable solution. For flows with complicated wave inter-



0021-9991/93 $5.00

actions such schemes may not be as robust as the shock-capturing schemes, even in one space dimension.

The research presented in this paper is part of a greater effort which aims to combine the characteristics of the above two categories of numerical schemes and to develop a method which will share the advantages and eliminate most of the disadvantages of both. This has been accomplished in the case of one-dimensional flow by the scheme presented in this paper. The increased accuracy which is provided in the computation of complicated wave interactions and its robustness have made this scheme especially valuable for the computation of reacting gas flows, where detonation waves are present.

The scheme is based on a conservative shock-capturing Godunov-type scheme, very much like van Leer's MUSCL scheme [15]. The new feature, introduced here, is an adaptive Lagrangian grid which increases the accuracy with which discontinuous waves and their interactions are computed. Without introducing additional computational elements, i.e., refining the grid, or special computational elements to represent these waves, the shocks and contact discontinuities are computed as true discontinuities, without the smearing effect typical of shock-capturing methods. This makes the scheme different from adaptive mesh refinement schemes (e.g., see Berger and Oliger [2]), which smear discontinuities, although on a much finer local grid. The basic conservative shock-capturing capabilities of the scheme are not diminished. The scheme is endowed with the capability to track various fronts and, thus, the shock-capturing and the front-tracking ideas are combined properly. It is important to note that the adaptive grid strategy, to a certain degree, is independent of the particular solver. Any Godunov-type scheme may be used. The Riemann solver is the link that provides the information about local wave interactions needed for the adaptive procedure.

It was deemed interesting to try this scheme on one-dimensional flows of reacting gases in light of the increased accuracy and robustness with which detonation waves and their interactions could be computed. The interest in such flows is evident by the number of papers appearing in the literature. For example, numerical calculations, with increased accuracy, of the one-dimensional instability of plane detonation waves may be of great interest in confirming existing theories which are based on linear stability analysis (e.g., see Lee and Stewart [9]). The present scheme is able to reduce the error caused by the numerical smearing of the leading shock of the detonation wave. This error may be very important in the development of detonation instability.

The computer code developed is also able to compute one-dimensional cylindrically and spherically symmetric flows, as well as plane flows with area change. It is thus possible to compute explosions and implosions and study the effect of curvature on detonation wave speed and stability. Most of the results presented are basically validation runs and calculations demonstrating the abilities of the method and the potential use for specific one-dimensional problems of interest. All results shown are for a perfect gas. The difficulty of incorporating a general equation of state is the same as in most schemes and independent of the main feature of the present scheme, i.e., the adaptive Lagrangian grid strategy.

## 2. NUMERICAL METHOD

### 2.1. *Mathematical Formulation*

The inviscid flow of a reacting mixture of calorically perfect gases is considered. The assumption of a simplified reacting mixture is made, according to which there are two species present at any time, the reactant and the product. The reactant is converted to the product by a one-step irreversible exothermic chemical reaction. This assumption is made in order to compare with the many theoretical and numerical results which are available in the literature for this case. The chemical reaction rate is given by the standard Arrhenius law

$$\dot{z} = -KzT^{\alpha} \exp(-E/R_g T), \tag{1a}$$

where $z$ is the mass fraction of unburnt gas, $K$ is a positive constant, which essentially gives a time scale, $E$ is the activation energy of the chemical reaction, $R_g$ is the gas constant, $T$ is the absolute temperature, and $\alpha$ is also a constant. The simplified Arrhenius model, where the reaction rate is a step function depending on the temperature, has also been used. For the simplified model the rate is given by

$$\dot{z} = -KzH(T - T_c), \tag{1b}$$

where

$$H(x) = \begin{cases} 1, & x > 0, \\ 0, & x \leqslant 0, \end{cases} \tag{2}$$

and $T_c$ is a given critical temperature.

The problem under consideration is a special case of the general problem of solving numerically the nonlinear hyperbolic system of the form

$$\frac{\partial U}{\partial t} + \frac{\partial F(U)}{\partial x} = G(U), \tag{3}$$

where $U$ is the appropriate solution vector. As usual, $x$ denotes the Eulerian space variable. If the Lagrangian formulation is used, a system of exactly the same form is

obtained. The space variable $x$, then, is replaced by a Lagrangian space variable and the flux vector $F(U)$ is changed appropriately. For non-reacting flow, $G(U)=0$. Most numerical methods use Eq. (3) as their starting point and, using a finite volume discretization, obtain the scheme of the following general form

$$U_j^{n+1} = U_j^n - \frac{\Delta t}{\Delta x}(\hat{F}_{j+1/2} - \hat{F}_{j-1/2}) + \Delta t\, \hat{G}_j, \tag{4}$$

giving the solution, in an average sense, in the $j$th cell at the time level $n+1$. The numerical flux terms $\hat{F}$ are computed at the boundaries of each cell. An important feature of every numerical method is the calculation of these flux terms in a way that guarantees stability and high-order accuracy.

A slightly different approach will be taken in deriving the present scheme. Eventually, it will be of the general form given in Eq. (4). It is useful to formulate the problem by writing the conservation laws in integral form for an arbitrary control volume $V(t)$, whose bounding surface $S(t)$ moves with a velocity $\mathbf{u}_b$ (Reynolds' transport theorem). These equations will be applied to each computational volume of the discrete numerical scheme. This is done so that the conservation equations and their discrete counterparts are written in a way which is independent of the Eulerian or Lagrangian formulation that will be adopted eventually. Moreover, it is easier to see from these equations how the idea for the adaptive nature of the grid is motivated. The conservation equations in integral form are

$$\frac{d}{dt}\int_{V(t)} \rho\, dV + \int_{S(t)} \rho(\mathbf{u}-\mathbf{u}_b)\cdot d\mathbf{S} = 0, \tag{5}$$

$$\frac{d}{dt}\int_{V(t)} \rho\mathbf{u}\, dV + \int_{S(t)} \rho\mathbf{u}(\mathbf{u}-\mathbf{u}_b)\cdot d\mathbf{S} + \int_{S(t)} p\, d\mathbf{S} = 0, \tag{6}$$

$$\frac{d}{dt}\int_{V(t)} \rho e_t\, dV + \int_{S(t)} \rho e_t(\mathbf{u}-\mathbf{u}_b)\cdot d\mathbf{S} + \int_{S(t)} p\mathbf{u}\cdot d\mathbf{S} = 0, \tag{7}$$

$$\frac{d}{dt}\int_{V(t)} \rho z\, dV + \int_{S(t)} \rho z(\mathbf{u}-\mathbf{u}_b)\cdot d\mathbf{S} - \int_{V(t)} \dot{z}\rho\, dV = 0. \tag{8}$$

These are written for an arbitrary control volume $V(t)$, whose bounding surface $S(t)$ has a velocity $\mathbf{u}_b$. In the above equations, $e_t$ is the total specific energy, which includes the chemical energy, i.e.,

$$e_t = e + \tfrac{1}{2}u^2 + q_0 z, \tag{9}$$

where $e$ is the specific internal energy, $q_0$ is the heat release of the chemical reaction, and $u=|\mathbf{u}|$ is the magnitude of the fluid velocity. The perfect gas assumption is also made, i.e.,

$$p = (\gamma - 1)\rho e. \tag{10}$$

Since the boundaries of the computational cells will be moving, it is useful to consider the flow map

$$\mathbf{x} = \mathbf{X}(\xi, t), \tag{11}$$

which gives the position of the fluid particle that was initially ($t=0$) at the position $\xi$. Thus, $\xi$ is convenient Lagrangian marker for the fluid particles in the flow. If the Lagrangian approach is taken, the local boundary velocity is equal to the local fluid velocity, i.e., $\mathbf{u}_b = \mathbf{u}$ in Eqs. (5)–(8).

### 2.2. *Spatial and Temporal Discretization*

Consider now the case of one-dimensional flow. A finite volume formulation is used, i.e., space is discretized by a set of computational cells as shown in Fig. 1. The conservation equations are now written for the $j$th cell of the computational grid

$$\frac{dm_j}{dt} + (\rho\,\Delta u_b)_{j+1/2} - (\rho\,\Delta u_b)_{j-1/2} = 0, \tag{12}$$

$$\frac{d}{dt}(m_j u_j) + (\rho u\,\Delta u_b)_{j+1/2} - (\rho u\,\Delta u_b)_{j-1/2} + p_{j+1/2} - p_{j-1/2} = 0, \tag{13}$$

$$\frac{d}{dt}(m_j e_{tj}) + (\rho e_t\,\Delta u_b)_{j+1/2} - (\rho e_t\,\Delta u_b)_{j-1/2} + (up)_{j+1/2} - (up)_{j-1/2} = 0, \tag{14}$$

$$\frac{d}{dt}(m_j z_j) + (\rho z\,\Delta u_b)_{j+1/2} - (\rho z\,\Delta u_b)_{j-1/2} - \dot{z}_j m_j = 0, \tag{15}$$

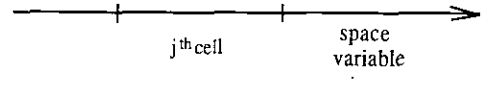


FIG. 1. Finite volume discretization in one space dimension. The space variable can be the Eulerian $x$ or the Lagrangian $\xi$. The boundaries of the $j$th cell are denoted by the subscripts $j \pm \frac{1}{2}$.

where

$$\begin{aligned} \Delta u_b &\equiv u - u_b, \\ m_j &\equiv \int_{x_{j-1/2}}^{x_{j+1/2}} \rho \, dx, \\ m_j u_j &\equiv \int_{x_{j-1/2}}^{x_{j+1/2}} \rho u \, dx, \\ m_j e_{tj} &\equiv \int_{x_{j-1/2}}^{x_{j+1/2}} \rho(e + \tfrac{1}{2}u^2 + q_0 z) \, dx, \\ m_j z_j &\equiv \int_{x_{j-1/2}}^{x_{j+1/2}} \rho z \, dx. \end{aligned} \tag{16}$$

Average values of all quantities in the $j$th cell are denoted by the subscript $j$ and values of various quantities at the two boundaries of the cell are denoted by the subscripts $j \pm \frac{1}{2}$. Note that average values are mass-averaged values. By defining

$$\begin{aligned} F_m &\equiv \rho \, \Delta u_b, \\ F_u &\equiv \rho u \, \Delta u_b + p, \\ F_e &\equiv \rho e_t \, \Delta u_b + p u, \\ F_z &\equiv \rho z \, \Delta u_b, \end{aligned} \tag{17}$$

the equations of motion can be written in the more familiar form

$$\begin{aligned} &\frac{dm_j}{dt} + (F_m)_{j+1/2} - (F_m)_{j-1/2} = 0, \\ &\frac{d}{dt}(m_j u_j) + (F_u)_{j+1/2} - (F_u)_{j-1/2} = 0, \\ &\frac{d}{dt}(m_j e_{tj}) + (F_e)_{j+1/2} - (F_e)_{j-1/2} = 0, \\ &\frac{d}{dt}(m_j z_j) + (F_z)_{j+1/2} - (F_z)_{j-1/2} = m_j \dot{z}_j. \end{aligned} \tag{18}$$

Note the extra degree of freedom provided in the flux terms by the, as of yet unspecified, term $\Delta u_b$. The motion of the cell boundaries is determined by

$$\frac{dx_{j\pm 1/2}}{dt} = (u_b)_{j\pm 1/2} \tag{19}$$

and the average density in each cell is given by

$$\rho_j = \frac{m_j}{x_{j+1/2} - x_{j-1/2}}. \tag{20}$$

The equation of state (10) provides the means for computing the average pressure in the $j$th cell,

$$p_j = (\gamma_j - 1)\, \rho_j \, (e_{tj} - q_0 z_j - \tfrac{1}{2} u_j^2). \tag{21}$$

The exact integral conservation laws have been written for each computational cell. Equations (18) will now be integrated in time explicitly. The basis for the method is a conservative Godunov-type scheme similar to the MUSCL scheme introduced by van Leer [15]. The procedure followed in solving these equations is similar to that used in most methods, which are higher-order extensions of the original Godunov scheme. At every time instant, average values of the solution are known in each computational cell. Linear variations of the primitive variables, i.e., density $\rho$, pressure $p$, and velocity $u$, are assumed in each cell. A Riemann problem is then set up locally at each cell interface. The solution to this problem gives the velocity, pressure and density needed to compute the flux terms (17). The different feature in the present scheme is that the Lagrangian formulation is used instead of the Eulerian and that an adaptive grid is used.

So far, the fact that the Lagrangian formulation is being used, has not appeared explicitly in the description of the method. It is now that this choice is made and all quantities are considered as functions of time $t$ and the Lagrangian space coordinate $\xi$. The interpolation procedure is carried out in $\xi$-space and, assuming linear variation, the generic quantity $q$ varies as

$$q(\xi) = q_j + (q_\xi)_j \, (\xi - \xi_j), \tag{22}$$

in the $j$th cell, where $q_j$ is the mass-averaged value in the cell, $\xi_j$ is the center of the cell (in Lagrangian space), and $(q_\xi)_j$ is the slope of $q$ in this cell, which is assumed to be constant. Note that discontinuities of these quantities are allowed at the cell interfaces, as shown in Fig. 2.

The slopes are chosen using the van Leer slope limiter [17], but the adaptive nature of the grid, which will be

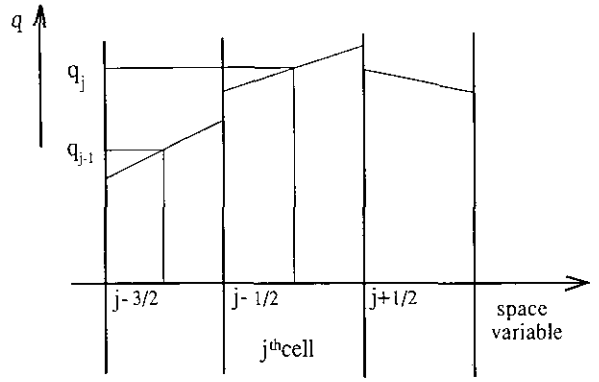


**FIG. 2.** Linear variation of the generic quantity $q$ in the $j$th cell. In general, $q$ is discontinuous at the cell interfaces.

described next, makes the choice of limiter less important than in the typical higher-order Godunov-type schemes. In fact, the adaptive grid allows more freedom in choosing the interpolation scheme, because additional information on the location of the various waves is always available at each time instant. The slope $(q_\xi)_j$ is computed, following van Leer [17], by

$$(q_\xi)_j = \text{ave}(q_\xi^-, q_\xi^+), \tag{23}$$

where

$$q_\xi^- = \frac{q_j - q_{j-1}}{\xi_j - \xi_{j-1}}, \quad q_\xi^+ = \frac{q_{j+1} - q_j}{\xi_{j+1} - \xi_j}, \tag{24}$$

$$\text{ave}(x, y) \equiv \frac{x+y}{2}\left[1 - \frac{(x-y)^2}{x^2+y^2+c^2}\right], \tag{25}$$

and $c^2$ is a small constant ($c^2 \ll 1$).

At each cell interface, two constant states $q^-$ and $q^+$ are required to be used as the initial condition for the Riemann problem. There are many ways of doing this. One way is to specify for the $j+\frac{1}{2}$ interface

$$\begin{aligned} q_{j+1/2}^- &= q_j + (q_\xi)_j\,(\xi_{j+1/2} - \xi_j), \\ q_{j+1/2}^+ &= q_{j+1} + (q_\xi)_{j+1}\,(\xi_{j+1/2} - \xi_{j+1}), \end{aligned} \tag{26}$$

i.e., the values of $q$ on either side of the interface, as given by Eq. (22). Using these states does not ensure second-order accuracy in time. The method used in the present scheme is shown in Fig. 3. The domain of dependence of $\xi = \xi_{j+1/2}$ over the time interval $\Delta t$ is estimated by the characteristics at the time level $t$. In the Lagrangian formulation of the problem the characteristic speeds are given by

$$c_\pm = \pm\frac{\rho}{\rho_0}a, \tag{27}$$

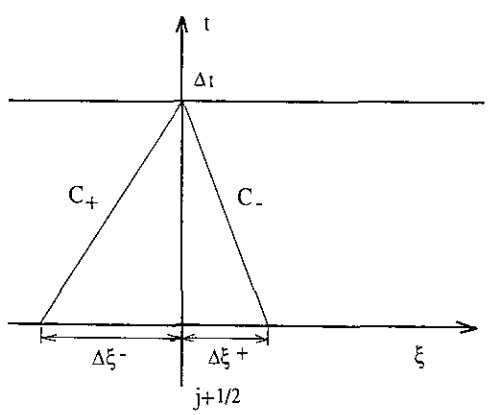


**FIG. 3.** The constant states $q^\pm$, which are to be used as the initial condition for the Riemann problem at the interface $j+\frac{1}{2}$, are obtained by averaging the linear interpolant over the domains of dependence $\Delta\xi^\pm$. These domains correspond to the full timestep $\Delta t$.

where $\rho_0$ is the initial density ($t=0$) and $a$ is the speed of sound. The constant states $q^\pm$ are then determined as the averages of Eq. (22) over the domains $\Delta\xi^\pm$; Fig. 3. These domains correspond to the full timestep $\Delta t$. This is equivalent to tracing the characteristics back from the time $t + \Delta t/2$ and using the linear profile (22). This ensures second-order accuracy in time.

The discrete scheme, giving the solution at the time level $n+1$ from the solution at the previous time level $n$, can now be written as

$$\begin{aligned} (m_j)^{n+1} &= (m_j)^n - \Delta t[(\hat{F}_m)_{j+1/2} - (\hat{F}_m)_{j-1/2}], \\ (m_j u_j)^{n+1} &= (m_j u_j)^n - \Delta t[(\hat{F}_u)_{j+1/2} - (\hat{F}_u)_{j-1/2}], \\ (m_j e_{tj})^{n+1} &= (m_j e_{tj})^n - \Delta t[(\hat{F}_e)_{j+1/2} - (\hat{F}_e)_{j-1/2}], \\ (m_j z_j)^{n+1} &= (m_j z_j)^n - \Delta t[(\hat{F}_z)_{j+1/2} - (\hat{F}_z)_{j-1/2}] \\ &\quad + \Delta t(m_j \dot{z}_j)^n, \\ x_{j\pm1/2}^{n+1} &= x_{j\pm1/2}^n + \Delta t(u_b)_{j\pm1/2}, \end{aligned} \tag{28}$$

where the numerical fluxes $\hat{F}_m$, $\hat{F}_u$, $\hat{F}_e$, and $\hat{F}_z$ are given by Eqs. (17), using the solution of the Riemann problem. The average boundary velocity $u_b$ for each interface is still unspecified, but for the majority of interfaces $u_b = u$ and the last of Eqs. (28) is second-order accurate in time. The source term in the species equation is shown in Eqs. (28) as being evaluated at the time level $n$. It is better to integrate the source term in a "split" manner, i.e., integrate the first four equations in (28) without the source term and use this intermediate state to estimate the term $m_j\dot{z}_j$. This splitting has been implemented in the present scheme.

The stability requirement on the timestep is that of a MUSCL scheme in the Lagrangian formulation. No additional stability problems arise due to the adaptive grid strategy presented in the next section.

### 2.3. *Adaptive Grid*

The motivation for the adaptive grid comes from the definition of the flux terms, as given by Eqs. (17). The term $\Delta u_b$, or, equivalently, the velocity of the cell boundary $u_b$, is unspecified. The idea is to specify it at each cell interface, so that all important discontinuous waves coincide with cell boundaries, at every discrete time level. The solution of the Riemann problem at a given interface provides all the information needed to identify all the important waves emanating from this interface, as well as their strengths and speeds. This information is enough to specify $\Delta u_b$. Since all important waves coincide with cell boundaries, it is guaranteed that, at subsequent time instants, the evolution of these waves will be determined properly by the solution of the

local Riemann problems. In the numerical experiments carried out, shock waves computed by the local Riemann solvers were considered important enough to track if the shock Mach number was greater than 1.01 and contact discontinuities were considered important if the ratio of the densities on either side was greater than 1.05. These parameters are quite conservative. One may want to track only the very strong shock waves in the flow.

The grid is, basically, Lagrangian, i.e., most cell boundaries move with the local fluid velocity and, hence $\Delta u_b = 0$. It is easy to see that the same ideas on the adaptivity of the grid can be used on a grid that is primarily Eulerian. The same equations can be applied directly.

An example of this adaptive procedure is shown in Fig. 4. A strong shock wave moving to the right is computed by the Riemann solver at the interface $i-\frac{1}{2}$ at time $t$. The decision is made to assign a velocity to the adjacent cell boundary $i+\frac{1}{2}$, so that at time $t+\Delta t$ the shock coincides with the interface $i+\frac{1}{2}$. Another possibility would be to have the interface $i-\frac{1}{2}$ move with the shock. The decision is made depending on which interface would be required to move a shorter distance in Lagrangian space. The shock speeds are assumed constant over the time interval $\Delta t$. It is obvious that the local expansion waves can be tracked in the same way. This was not implemented in the present scheme, simply to reduce the complexity of the programming.

It is evident from this example that a relation between the velocities in real space and the velocities in Lagrangian space is needed to update the Lagrangian grid. Consider the motion of a cell boundary given by the trajectory $x = x_b(t)$. This boundary is moving with a velocity $u_b = \dot{x}_b(t)$, which, in general, is different from that of the fluid $u$. This motion corresponds to a motion in $\xi$-space given by the trajectory $\xi = \xi_b(t)$ with velocity $v_b = \dot{\xi}_b(t)$. The relation between the two velocities is found with the use of the flow map

$$x = X(\xi, t), \tag{29}$$

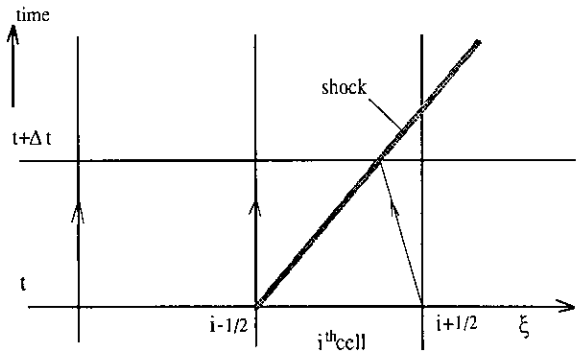


**FIG. 4.** The appropriate velocity is assigned to the cell interface $i+\frac{1}{2}$ in order to intercept the shock at the subsequent discrete time level.

which is essentially Eq. (11) written here for one-dimensional flow. The cell boundary motion is given by

$$x_b(t) = X(\xi_b(t), t) \tag{30}$$

and, hence,

$$u_b = \left(\frac{\partial X}{\partial t}\right)_\xi + \dot{\xi}_b(t)\left(\frac{\partial X}{\partial \xi}\right)_t \tag{31a}$$

or

$$u_b = u + v_b\left(\frac{\partial X}{\partial \xi}\right)_t. \tag{31b}$$

The derivative of the flow map is numerically approximated and assumed constant in each cell, i.e.,

$$\left(\frac{\partial X}{\partial \xi}\right)_j \simeq \frac{x_{j+1/2} - x_{j-1/2}}{\xi_{j+1/2} - \xi_{j-1/2}}. \tag{32}$$

The velocities of the various waves, which are computed by the Riemann problems, can be translated into velocities in $\xi$-space by using Eq. (31b). The Lagrangian position of each interface is updated by

$$\xi^{n+1}_{j\pm 1/2} = \xi^n_{j\pm 1+2} + \Delta t (v_b)_{j\pm 1/2}. \tag{33}$$

The solution to the Riemann problem at each interface provides sufficient information for the adaptive strategy. Using the exact Riemann solver at every interface is very costly. To reduce the cost, various criteria were found to identify the cell interfaces where a strong discontinuous wave is suspected to be present, before solving the Riemann problem. These interfaces are flagged as critical interfaces. The ratio $\Delta\xi^-/\Delta\xi^+$ has proven useful in detecting developing shocks in the flow. Where the flow is smooth, without steep gradients, the above ratio is

$$\frac{\Delta\xi^-}{\Delta\xi^+} \simeq 1. \tag{34}$$

The regions, where this ratio deviates from unity by more than 10%, are considered critical regions. The full nonlinear Riemann solver is used only in these regions. Everywhere else the simple acoustic approximation to the Riemann problem solution is used. It was found in all the numerical experiments performed that, in addition to the above criterion, finding local extrema of the slopes in pressure, density, and velocity was very useful in determining these regions. Other criteria may also be used. It is important that the criteria be conservative enough, so that no critical regions are missed, but they are not crucial in detecting

discontinuous waves. The detection of important discontinuous waves is ultimately done by examining the solutions to the local Riemann problems.

No more than two adjacent critical interfaces are allowed at any given time. In the smooth compression regions, the interfaces at the maxima of the pressure gradients are considered critical. The pressure gradients are estimated using simple finite differences. If the Riemann solver at these locations computes sufficiently strong discontinuous waves, then they are tracked. The critical interfaces, which carry these waves, are treated the same way at the next time level along with other possible critical interfaces that may be detected. When there are two adjacent critical interfaces, the two Riemann problems are solved simultaneously. At this point it is decided if collisions will occur within the timestep $\Delta t$. There are six waves resulting from the two Riemann problems and there are four cell interfaces available to do the tracking. The strongest waves are tracked and the others are ignored. This procedure has proven to be very robust in handling all possible wave interactions.

Collisions and reflections from walls can be treated in a straightforward way using this adaptive grid. A typical collision case is shown in Fig. 5. At time $t$, two strong shock waves at the interfaces $i-\frac{1}{2}$ and $i+\frac{1}{2}$, are moving at each other with speeds that allow for a collision before time $t+\Delta t$. The Riemann problems at the interfaces $i-\frac{1}{2}$ and $i+\frac{1}{2}$ are solved at time $t$, simultaneously. The solution indicates that there will be a collision within the time interval $\Delta t$. The time step is adjusted locally, i.e., only for the three cells $i-1$, and $i+1$, so that at the intermediate time instant the collision point coincides with the cell boundary $i+\frac{1}{2}$. The Riemann solver at this interface, at the intermediate time instant, will compute the two shock waves emerging from the collision and the adjacent cell boundaries will be able to track them in the same way at subsequent times. The fluxes at the interfaces $i-\frac{3}{2}$ and $i+\frac{3}{2}$ are held constant for the whole timestep $\Delta t$. This leads to a robust way of handling wave interactions, without loss of accuracy.

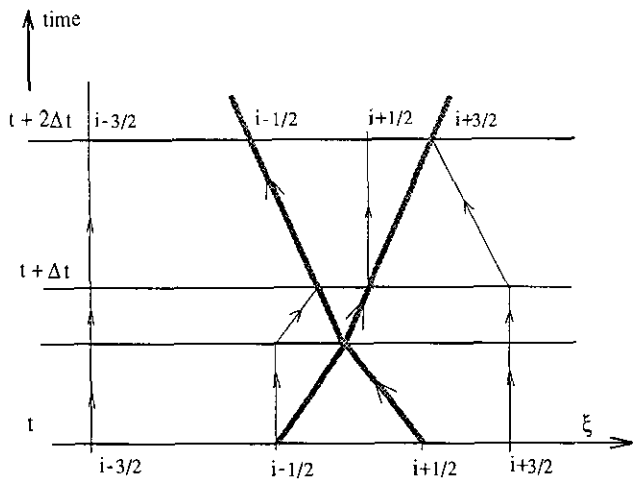


**FIG. 5.** The typical collision of two shocks is shown. The time step is adjusted locally so that the collision point coincides with the cell interface $i+\frac{1}{2}$ at the intermediate time step.

## 3. RIEMANN SOLVER

The Riemann solver is an important ingredient of the numerical scheme. It provides the means for computing the velocity and the pressure at the cell interfaces and, thus, the various flux terms required. It also gives valuable information about the local waves emanating from each cell interface. As explained in the previous section, the Lagrangian grid adapts in such a way that important discontinuous waves and collision points coincide with cell boundaries at each time instant. It is, therefore, necessary to be able to identify the waves emanating from these critical cell boundaries at subsequent times. This is what the Riemann solver accomplishes. A variety of exact and approximate Riemann solvers have appeared in the literature in recent years. In all these solvers the focus is on computing the velocity and pressure of the contact discontinuity, which appears after the breakup of the initial discontinuity of the Riemann problem. In the present scheme it is crucial to identify the exact wave pattern as well. This information is used to assign the appropriate velocities to adjacent cell boundaries so that all important waves are tracked and to adjust the time step locally so that collisions are computed accurately. Moreover, the fluxes at an interface need to be computed along the ray $\dot{\xi}(t)=v_b$; see Eq. (31b). Most interfaces are Lagrangian and hence, $v_b=0$.

### 3.1. *Non-reacting Perfect Gas*

Consider the case of the Riemann problem for inviscid flow of a perfect gas without chemical reactions. The initial condition at time $t=0$ consists of two constant states denoted by the subscripts $r$ and $l$. Note that it is possible to have two different perfect gases on either side of the $\xi=0$ location, as indicated by the different specific heat ratios, i.e., $\gamma_r$ and $\gamma_l$; see Fig. 6. The space variable $\xi$ is the

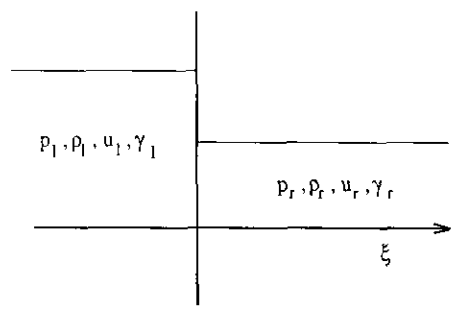


**FIG. 6.** Initial condition for the Riemann problem. The variable $\xi$ is the Lagrangian space coordinate.

Lagrangian space coordinate. At time $t=0^+$ the general wave pattern shown in Fig. 7 will develop.

There is a wave moving to the right (positive $\xi$) denoted by $R$, a wave moving to the left (negative $\xi$) denoted by $L$, and a contact discontinuity $C$ which remains at $\xi=0$ for all time, i.e., moves with the local fluid velocity. The waves $R$ and $L$ are either shocks or expansion waves, depending on the initial condition. Across the contact discontituity $C$ the pressure $p_f$ and velocity $u_f$ are continuous, but the density has a jump discontinuity at $\xi=0$ for all time. The density is $\rho_{fl}$ for $\xi<0$ and $\rho_{fr}$ for $\xi>0$. It is known that the solution to this initial value problem exists and is unique for arbitrary initial conditions. Moreover, the solution is self-similar and the shock waves propagate with a constant velocity and strength. That is why they are represented by straight lines in the $(\xi, t)$ diagram.

There are four wave patterns possible for this problem. The solution will be found for each of these wave patterns for the special case of a perfect gas.

(i) *L-shock, R-shock.* Across the shock $R$ the following relationship holds:

$$r\equiv\frac{u_f-u_r}{a_r}=\frac{2}{\gamma_r+1}\left(M_r-\frac{1}{M_r}\right). \tag{35}$$

$M_r$ is the shock Mach number defined by

$$M_r\equiv\frac{U_r-u_r}{a_r}, \tag{36}$$

where $U_r$ is the shock velocity and $a_r=\sqrt{\gamma_r p_r/\rho_r}$ is the speed of sound in the undisturbed region $r$. Similarly for the shock $L$,

$$\frac{u_l-u_f}{a_l}=\frac{2}{\gamma_l+1}\left(M_l-\frac{1}{M_l}\right). \tag{37}$$

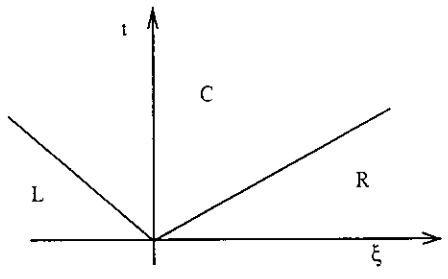


**FIG. 7.** General wave pattern resulting from the breakup of the original discontinuity of the Riemann problem. $C$ is a contact discontinuity. $L$ and $R$ can be either shocks or expansion waves.

where $M_l$ is the shock Mach number for $L$. Equations (35) and (37) can be solved for the shock Mach numbers to give

$$M_r=\frac{\gamma_r+1}{4}r+\sqrt{\left(\frac{\gamma_r+1}{4}\right)^2 r^2+1}, \tag{38}$$

$$M_l=\frac{\gamma_l+1}{4}\frac{u_l-u_f}{a_l}+\sqrt{\left(\frac{\gamma_l+1}{4}\right)^2\left(\frac{u_l-u_f}{a_l}\right)^2+1}. \tag{39}$$

The pressure ratios across the two shocks are given by the equations

$$\frac{p_f}{pr}=1+\frac{2\gamma_r}{\gamma_r+1}(M_r^2-1), \tag{40}$$

$$\frac{p_f}{p_l}=1+\frac{2\gamma_l}{\gamma_l+1}(M_l^2-1). \tag{41}$$

From Eqs. (38)–(41) one obtains a single equation for the unknown $r$,

$$\begin{aligned}G(r)\equiv 1-\frac{p_l}{p_r}+\gamma_r\frac{\gamma_r+1}{4}r^2+\gamma_r r\sqrt{\left(\frac{\gamma_r+1}{4}\right)^2 r^2+1}\\ -\frac{p_l}{p_r}\gamma_l\frac{\gamma_l+1}{4}\left(\frac{u_l-u_r}{a_l}-\frac{a_r}{a_l}r\right)^2\\ -\frac{p_l}{p_r}\gamma_l\left(\frac{u_l-u_r}{a_l}-\frac{a_r}{a_l}r\right)\\ \times\sqrt{\left(\frac{\gamma_l+1}{4}\right)^2\left(\frac{u_l-u_r}{a_l}-\frac{a_r}{a_l}r\right)^2+1}=0.\end{aligned} \tag{42}$$

This equation is solved numerically using a Newton–Raphson method. Once $r$ is obtained, all other quantities of interest follow from Eqs. (35)–(41). The densities are determined by

$$\frac{\rho_{fi}}{\rho_i}=\frac{(\gamma_i+1)M_i^2}{2+(\gamma_i-1)M_i^2},\qquad i=r, l. \tag{43}$$

It is important to be able to determine if this wave pattern will develop for a given initial condition. For this solution to be possible, certain compatibility conditions must hold. These are easily found by noticing that in Eqs. (35) and (37) the shock Mach numbers $M_r$ and $M_l$ must be greater than 1. It then follows that the following compatibility condition

$$u_r\leqslant u_f\leqslant u_l \tag{44}$$

must hold or, equivalently,

$$u_r - u_l \leqslant 0,$$
$$0 \leqslant r \leqslant \frac{u_l - u_r}{a_r}. \tag{45}$$

(ii) *L-expansion wave, R-shock.* In this case, Eqs. (35), (36), (38), and (40), derived previously, still hold for the shock wave $R$. In addition to these equations, the following equation gives the pressure ratio across the isentropic expansion wave,

$$\frac{p_f}{p_l} = \left(1 + \frac{\gamma_l - 1}{2}\frac{u_l - u_f}{a_l}\right)^{2\gamma_l/(\gamma_l - 1)}$$
$$= \left(1 + \frac{\gamma_l - 1}{2}\frac{u_l - u_r}{a_l} - \frac{\gamma_l - 1}{2}\frac{a_r}{a_l}r\right)^{2\gamma_l/(\gamma_l - 1)}, \tag{46}$$

where $r$ is defined in Eq. (35). Combining Eqs. (38), (40), and (46), a single equation in $r$ is obtained, as in the previous case,

$$F(r) \equiv 1 + \gamma_r \frac{\gamma_r + 1}{4} r^2 + \gamma_r r \sqrt{\left(\frac{\gamma_r + 1}{4}\right)^2 r^2 + 1}$$
$$- \frac{p_l}{p_r}\left(1 + \frac{\gamma_l - 1}{2}\frac{u_l - u_r}{a_l} - \frac{\gamma_l - 1}{2}\frac{a_r}{a_l}r\right)^{2\gamma_l/(\gamma_l - 1)} = 0, \tag{47}$$

which is solved numerically. The densities are determined by Eq. (43) across the shock and by the isentropic relation

$$\frac{\rho_{fl}}{\rho_l} = \left(\frac{p_{fl}}{p_l}\right)^{1/\gamma},$$

across the expansion wave.

The compatibility conditions are found by noting that across the expansion wave $L$, $0 \leqslant p_f/p_l \leqslant 1$ and across the shock $R$, $p_f/p_r \geqslant 1$. Using Eqs. (40) and (46) the following relations are found, after some algebra,

$$p_r/p_l \leqslant 1,$$
$$u_r - u_l < \left(\frac{2}{\gamma_l - 1}\right) a_l, \tag{48}$$

and

$$\frac{u_l - u_r}{a_r} \leqslant r < \frac{u_l - u_r}{a_r} + \left(\frac{2}{\gamma_l - 1}\right)\frac{a_l}{a_r}$$
$$0 \leqslant r.$$

(iii) *L-shock, R-expansion wave.* This case is exactly the same as case (ii) with the transformation $\xi \to -\xi$.

(iv) *L-expansion wave, R-expansion wave.* In this case, there are two expansion waves and the pressure ratios across them are given by

$$\frac{p_f}{p_l} = \left(1 + \frac{\gamma_l - 1}{2}\frac{u_l - u_f}{a_l}\right)^{2\gamma_l/(\gamma_l - 1)},$$
$$\frac{p_f}{p_r} = \left(1 + \frac{\gamma_r - 1}{2}\frac{u_f - u_r}{a_r}\right)^{2\gamma_r/(\gamma_r - 1)}. \tag{50}$$

From Eqs. (50) the following single equation in $r$ is obtained,

$$S(r) \equiv \left(1 + \frac{\gamma_r - 1}{2}r\right)^{2\gamma_r/(\gamma_r - 1)}$$
$$- \frac{p_l}{p_r}\left(1 + \frac{\gamma_l - 1}{2}\frac{u_l - u_r}{a_l} - \frac{\gamma_l - 1}{2}\frac{a_r}{a_l}r\right)^{2\gamma_l/(\gamma_l - 1)} = 0, \tag{51}$$

which is solved numerically with the Newton–Raphson method. The compatibility conditions are once again found by noting that across the expansion waves $0 \leqslant p_f/p_l \leqslant 1$ and $0 \leqslant p_f/p_r \leqslant 1$, which, using Eqs. (50), give

$$0 \leqslant u_r - u_l < 2\left(\frac{a_r}{\gamma_r - 1} + \frac{a_l}{\gamma_l - 1}\right) \tag{52}$$

and

$$-\frac{2}{\gamma_r - 1} < r \leqslant 0,$$
$$\frac{u_l - u_r}{a_r} \leqslant r < \frac{u_l - u_r}{a_r} + \left(\frac{2}{\gamma_l - 1}\right)\frac{a_l}{a_r}. \tag{53}$$

### 3.2. *Acoustic Approximation*

The solution to the Riemann problem becomes easier to obtain when the initial conditions are such that the waves $R$ and $L$ shown in Fig. 7 are so weak that linear acoustic theory can be used. This happens when the distance, in some sense, between the two constant states $r$ and $l$ is small. The waves $R$ and $L$ can then be treated as acoustic waves with the pressure ratios across them given by the simple relations,

$$p_f = p_r + \sqrt{\gamma_r p_r \rho_r}\,(u_f - u_r), \tag{54a}$$
$$p_f = p_l - \sqrt{\gamma_l p_l \rho_l}\,(u_f - u_l). \tag{54b}$$

Combining Eqs. (54a) and (54b), one finds

$$u_f = (p_l - p_r + \sqrt{\gamma_r p_r \rho_r}\,u_r + \sqrt{\gamma_l p_l \rho_l}\,u_l)/(\sqrt{\gamma_r p_r \rho_r} + \sqrt{\gamma_l p_l \rho_l}). \tag{55}$$

The densities behind these waves are given by

$$\rho_{fi} = \rho_i(p_f + \mu_i^2 p_i)/(p_i + \mu_i^2 p_i), \tag{56}$$

where

$$\mu_i^2 \equiv (\gamma_i - 1)/(\gamma_i + 1), \quad i = r, l. \tag{57}$$

### 3.3. *Reacting Mixture of Calorically Perfect Gases*

So far, the classical Riemann problem for non-reacting inviscid flow has been considered. The solution to this problem, as mentioned before, is a self-similar solution, i.e., depending on $x/t$ only. For the case of a simple reacting mixture the nonlinear system of equations, that needs to be solved, is of the form

$$\frac{\partial U}{\partial t} + \frac{\partial F(U)}{\partial x} = G(U), \tag{58}$$

where

$$U = \begin{pmatrix} \rho \\ \rho u \\ \rho(e + \frac{1}{2}u^2) \\ \rho z \end{pmatrix}, \quad F(U) = \begin{pmatrix} \rho u \\ \rho u^2 + p \\ \rho u(e + \frac{1}{2}u^2) + pu \\ \rho z u \end{pmatrix} \tag{59}$$

and

$$G(U) = \begin{pmatrix} 0 \\ 0 \\ 0 \\ -\rho \dot{z} \end{pmatrix}. \tag{60}$$

This is written using the Eulerian formulation, but one obtains a system of exactly the same form, if the Lagrangian formulation is used. The Riemann problem solution, described so far, is for the non-reacting case, i.e., $G(U) = 0$. For the reacting case, jumps in the concentration of unburnt gas $z$ are allowed only across contact discontinuities, but not across shocks. The solution to this problem is more complicated and no longer self-similar. In Fig. 8, a typical wave pattern is shown. The shock and expansion waves are curved in the $(\xi, t)$ plane; i.e., they are accelerating. The solution to this generalized Riemann problem has been worked out by Matania Ben-Artzi [1]. It is shown that the solution approaches the solution of the classical Riemann problem for the non-reacting case in the limit $\xi \to 0$ and $t \to 0$. The more complicated generalized Riemann solver given by Ben-Artzi provides higher order accuracy over the usual non-reacting solver. Numerical experiments were performed using the present adaptive Lagrangian scheme with both Riemann solvers. It was found that the simpler solver gave results which were just as good. The acceleration of the various waves was captured numerically quite accurately.

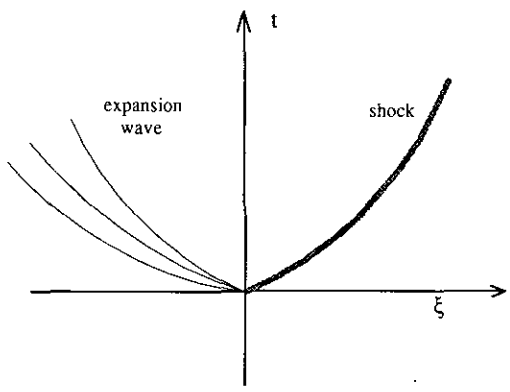


**FIG. 8.** This is a typical wave pattern resulting from the breakup of the initial discontinuity of the Riemann problem for the case of a simple reacting mixture. The solution is no longer self-similar.

## 4. NUMERICAL RESULTS

A number of test cases were run using this numerical scheme. The cases were chosen primarily to validate the code and to demonstrate its potential for solving 1D problems with complicated wave interactions. The scheme is particularly useful for computing unsteady reacting flows involving detonation waves and their interactions.

### 4.1. *Sod's Shock-Tube Problem*

The first case is the classical shock-tube problem. It is an important validation run for the code. The initial conditions used are those proposed by Sod [13]. At time $t = 0$ a diaphragm at the location $x = 0.5$ separates the two constant states

$$\begin{aligned} p_l &= 1.0, \quad \rho_l = 1.0, \quad u_l = 0.0, \quad x < 0.5 \\ p_r &= 0.1, \quad \rho_r = 0.125, \quad u_r = 0.0, \quad x > 0.5, \end{aligned} \tag{61}$$

for a perfect gas with $\gamma = 1.40$. $N = 150$ computational cells are used in this calculation. In all the results presented, the solutions are given as functions of the Eulerian space variable $x$, even though the calculation is done in Lagrangian space. The Lagrangian aspect of the scheme is evident by the increased density of computational points in compression regions. The comparison between the numerical solution and the exact solution shown in Fig. 9 is excellent. Note that the expansion wave is computed with the accuracy of typical shock-capturing schemes, since no effort is made to track expansion waves. The shock wave and the contact discontinuity are computed with no smearing.

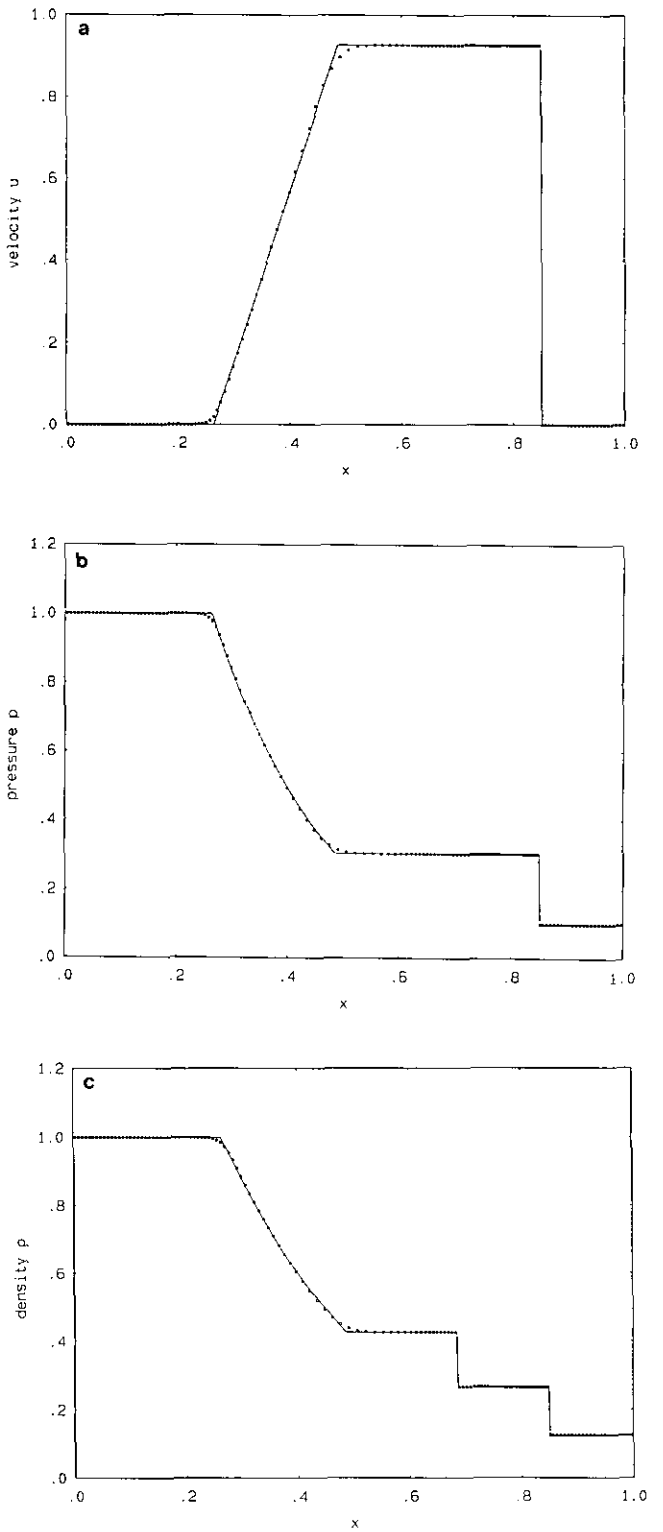


**FIG. 9.** (a) Velocity profile at time $t = 0.20$ for Sod's shock tube problem with $N = 150$ computational cells. (b) Pressure profile at time $t = 0.20$ for Sod's shock tube problem with $N = 150$ computational cells. (c) Density profile at time $t = 0.20$ for Sod's shock tube problem with $N = 150$ computational cells. The solid lines represent the exact solutions and the boxes represent the numerical solutions.

In order to demonstrate the ability of the scheme to compute complicated wave interactions accurately, the shock tube problem is carried a step further. Reflecting walls are assumed present at the locations $x = 0$ and $x = 1$. The computation is continued to see how the multiple reflections of the shock from the walls and its collisions with the contact discontinuity are calculated. In Fig. 10, the solution is shown after the first reflection of the shock wave from the wall at $x = 1$, which occurs at $t = 0.285$. In Fig. 11, the reflected shock has collided with the contact discontinuity and a new shock wave has been generated. The solution at a later time is shown in Figs. 12. The computation was carried out until time $t = 7.88$. That corresponds to many reflections of the original shock. In a real experiment viscous effects would have made the process die down much sooner. In Fig. 13, the entropy of the system is shown as a function of time. The entropy is defined by

$$s \equiv \ln(p/\rho^{\gamma}). \tag{62}$$

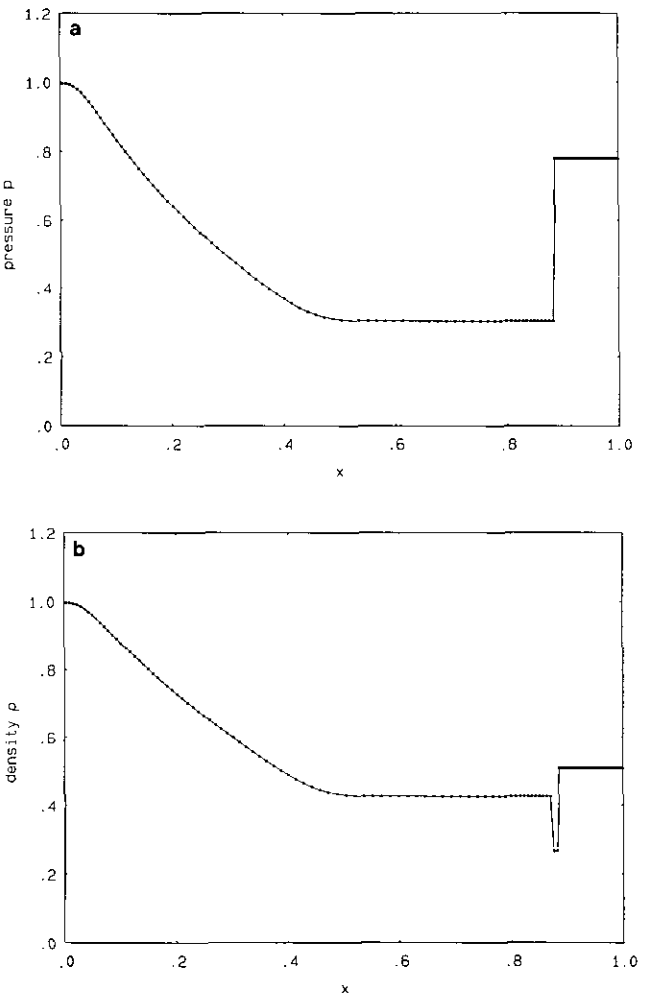


**FIG. 10.** (a) Pressure profile at time $t = 0.40$. (b) Density profile at time $t = 0.40$. The shock has reflected from the wall at $x = 1$.

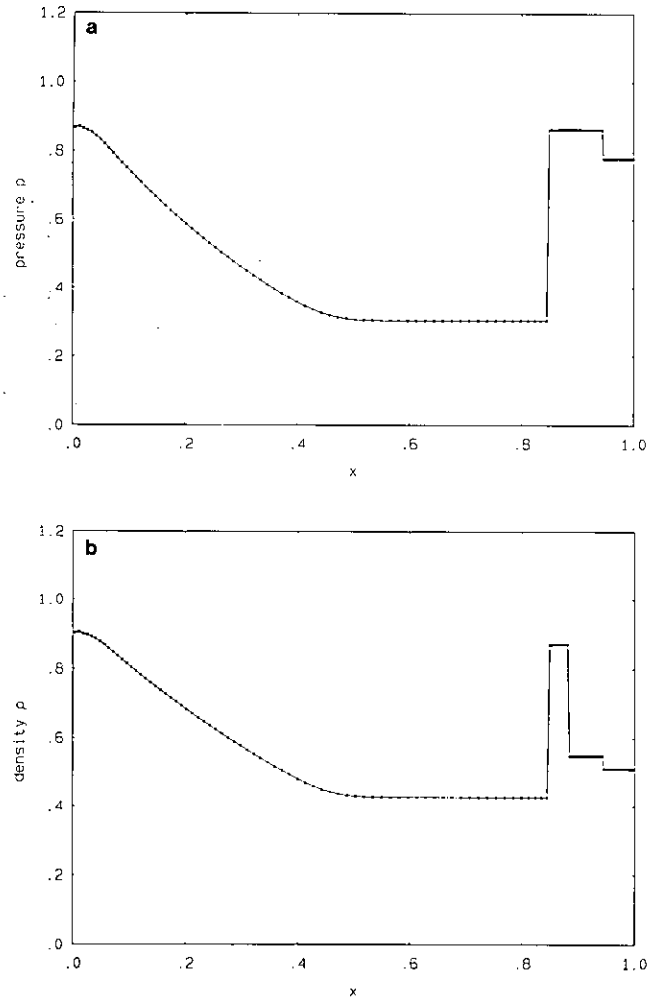


FIG. 11. (a) Pressure profile at time $t = 0.45$. (b) Density profile at time $t = 0.45$. The reflected shock has collided with the contact discontinuity. A secondary shock has been generated.

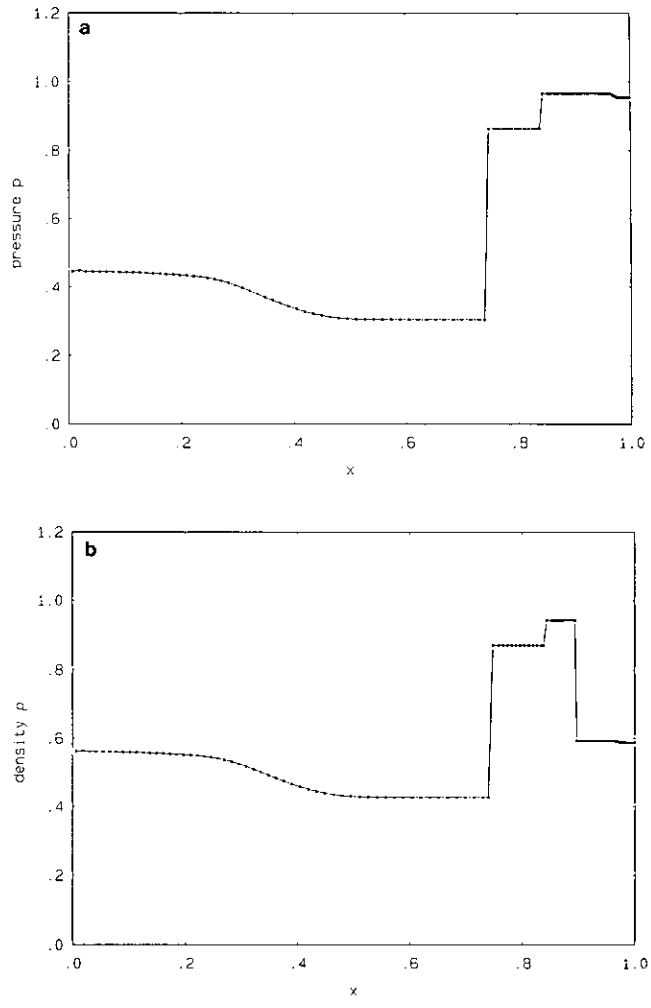


FIG. 12. (a) Pressure profile at time $t = 0.61$. (b) Density profile at time $t = 0.61$. An acoustic wave has been generated from the collision of the secondary shock with the contact discontinuity.

As $t \to \infty$, the system approaches the state predicted by thermodynamics, since the scheme is fully conservative. Any scheme which conserves total mass and energy will give the correct final entropy. In this case it is $s = 0.1168$ in the appropriate dimensionless units. This is an important point worth repeating here. The conservative character of the scheme is not compromised by the use of the adaptive grid technique.

## 4.2. *Strong Shock Wave Problem*

The strong shock wave problem used by Woodward and Colella [18] is computed with the present scheme. This problem is a good test case because of the strong interacting discontinuous waves. The initial condition is that of a gas

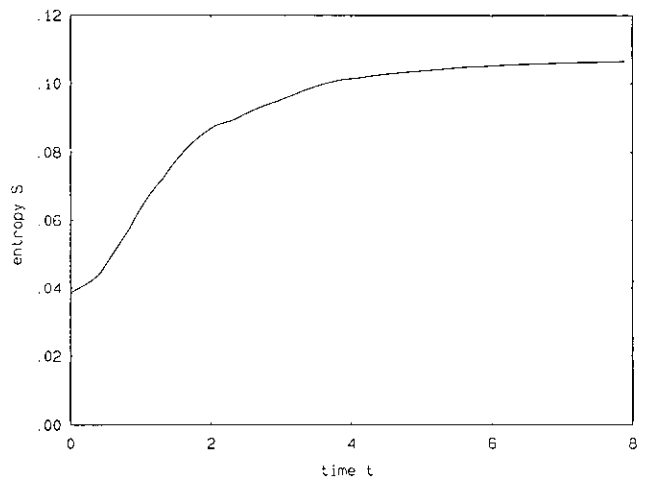


FIG. 13. Entropy $s = \ln(p/\rho^{\gamma})$ of the system as a function of time for the shock tube problem with multiple reflections.

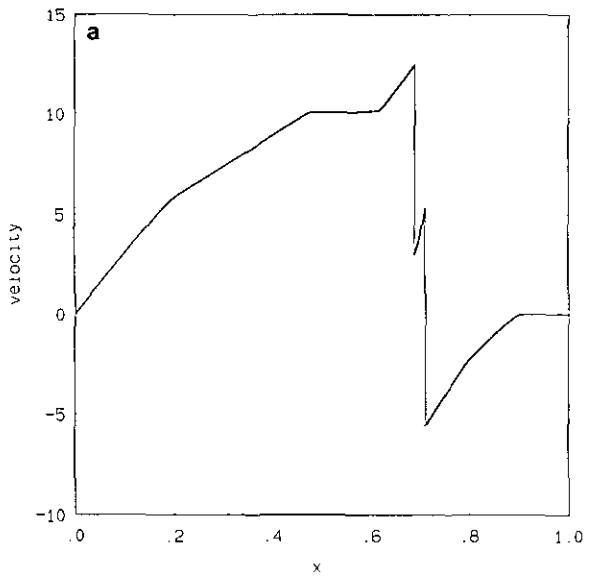


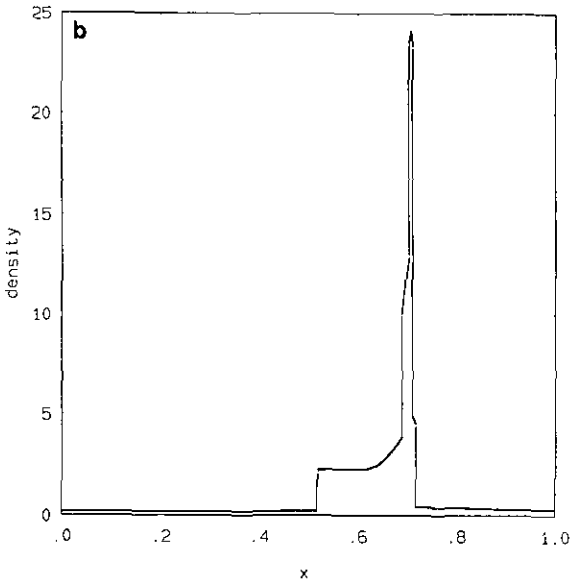


FIG. 14. (a) Velocity profile and (b) density profile at time $t = 0.030$ for the strong shock wave problem.

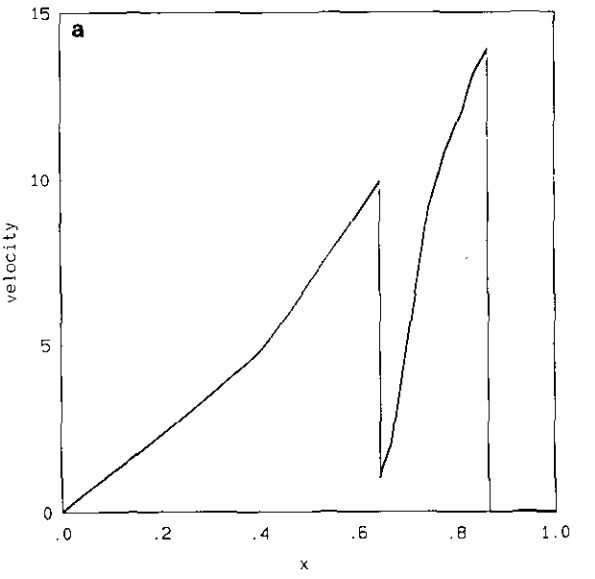


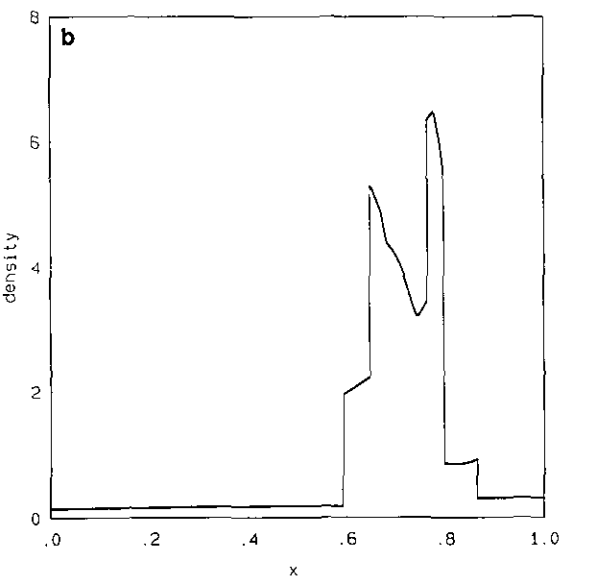


FIG. 15. (a) Velocity profile and (b) density prifile at time $t = 0.038$ for the strong shock wave problem.

with specific heat ratio $\gamma = 1.4$ at rest in the tube $0 \leqslant x \leqslant 1$. The initial density is $\rho = 1$ and the pressure is

$$\begin{aligned} p &= 1000, \quad x < 0.1, \\ p &= 0.01, \quad 0.1 < x < 0.9, \\ p &= 100, \quad 0.9 < x < 1. \end{aligned} \tag{63}$$

The results are shown in Figs. 14 and 15 for the times $t = 0.030$ and $t = 0.038$, respectively; 800 computational cells were used for this calculation.

### 4.3. *ZND Detonation Waves*

Another test case is that of a steady detonation wave. The well-known ZND theory (Zel'dovich–VonNeumann–Doering) for a steady detonation is used to compare with the numerical solution obtained using this scheme. As a first check, the profile of a steady detonation wave, computed using the ZND theory, is given as the initial condition to the unsteady code. The solution after time $t = 10$ (10,000 time steps) is then superimposed on the ZND solution and compared. The comparison, shown in Fig. 16, is excellent.

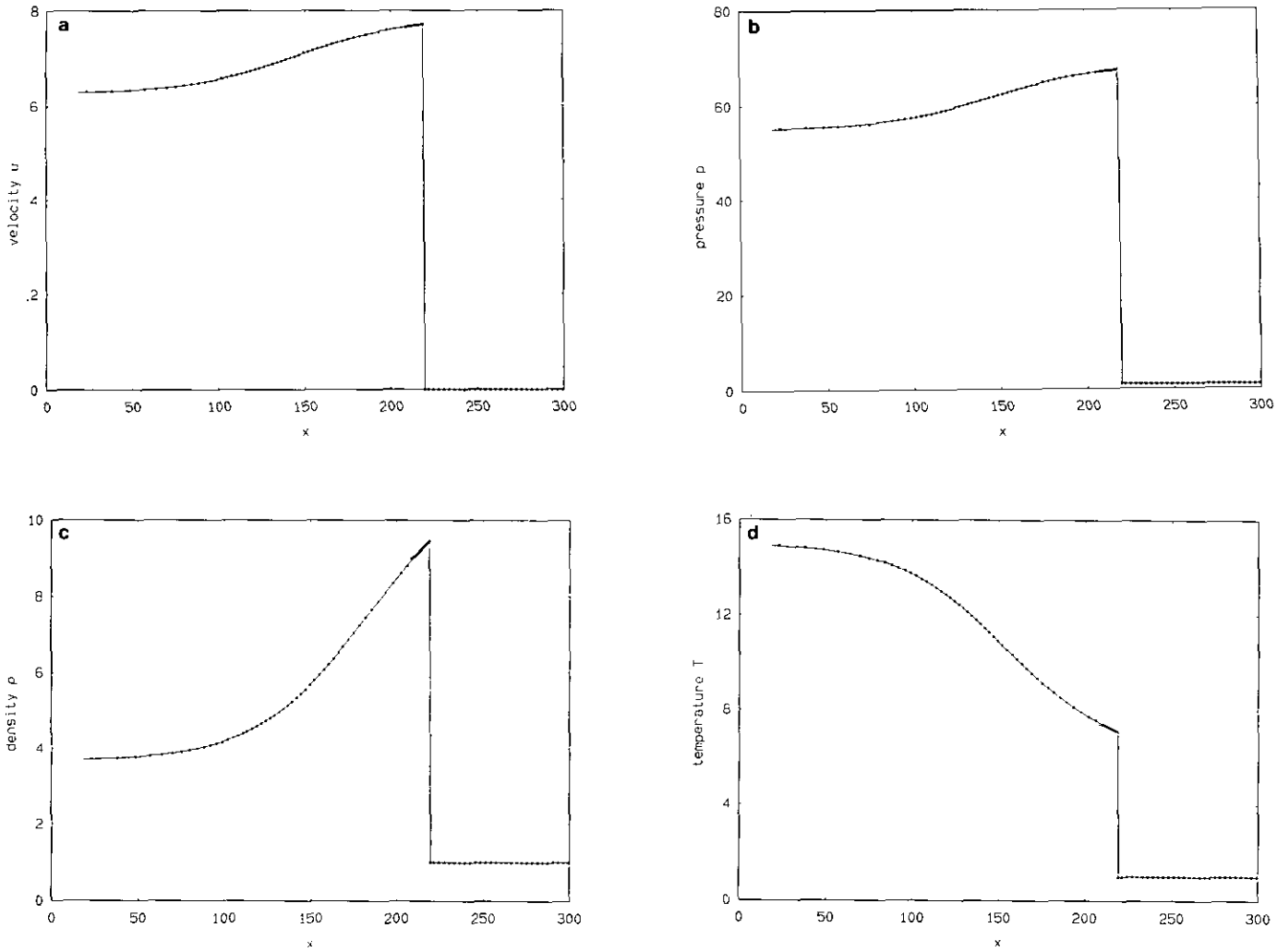


**FIG. 16.** (a) Velocity profile at $t = 10$. (b) Pressure profile at $t = 10$. (c) Density profile at $t = 10$. (d) Temperature profile at $t = 10$. The solid lines are the solutions given by the ZND theory. The boxes are the numerical solutions.

The standard Arrhenius law, given by Eq. (1a), is used for the chemical reaction rate with $\alpha = 0$, i.e.,

$$\dot{z} = -KzT^{\alpha} \exp(-E/R_g T).$$

The parameters used for this test run are

$$\gamma = 1.2, \quad q_0/R_g T_0 = 50, \quad E/R_g T_0 = 40,$$

where the subscript zero denotes the undisturbed region into which the detonation propagates. This steady detonation wave corresponds to an overdrive factor of $f = 1.6$. The overdrive factor is defined by

$$f = D^2/D_{CJ}^2,$$

where $D$ is the detonation wave speed and $D_{CJ}$ is the detonation speed corresponding to the Chapman–Jouguet point. For details on the ZND theory see the book by Fickett and Davis [4].

The case of unsteady detonation waves will now be considered. For the following cases the simplified Arrhenius chemical rate law is used (Eq. (1b)), i.e.,

$$\dot{z} = -KzH(T - T_c),$$

where $T_c$ is a critical temperature above which the chemical reaction begins. Figure 17 shows the evolution of an unsteady detonation propagating in an undisturbed region. It is the well-known piston problem. The motion of the piston, starting at $x = 0$, generates a shock which raises the temperature of the gas above the critical value $T_c$. The chemical reaction begins and the detonation wave

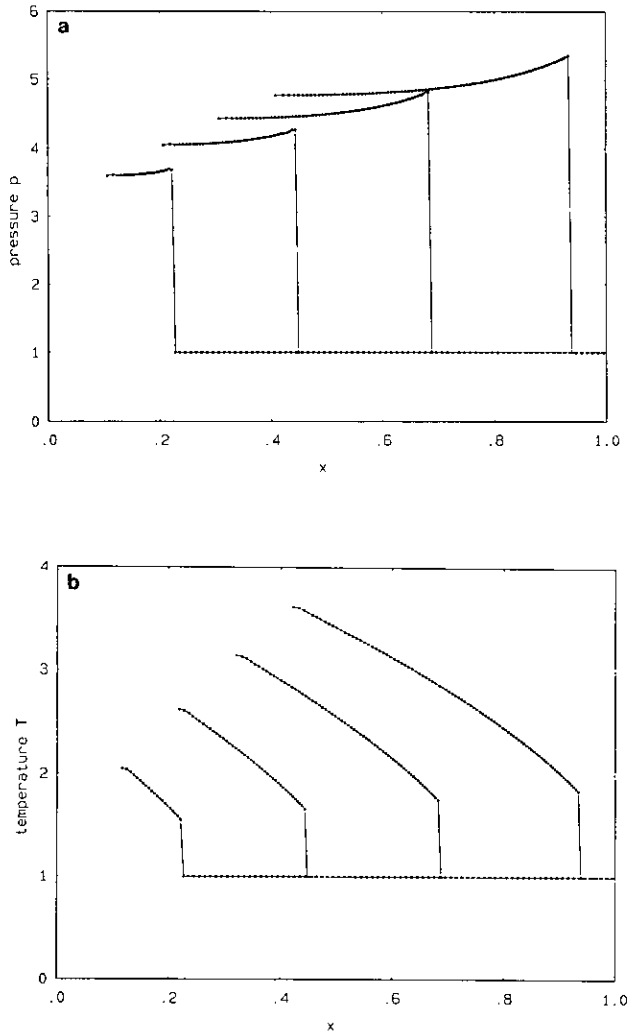


**FIG. 17.** (a) Pressure profiles for the piston problem. (b) Temperature profiles for the piston problem. The detonation waves generated accelerate into the undisturbed region. In this case the critical temperature is $T_c = 1.3$; times $t = 0.1, 0.2, 0.3, 0.4$.

accelerates into the undisturbed region. The numerical values used in this run are

$$\gamma = 1.4, \quad q_0 = 20, \quad T_c = 1.3,$$

where all quantities are normalized with the corresponding values in the undisturbed region. The piston velocity is taken to be $u_p = 1$.

A more interesting case is shown in Fig. 18. The initial condition is a smooth pressure distribution with zero initial velocity, which leads to isentropic compression and, eventually, shock formation. If in this compression the temperature of the gas becomes larger than $T_c$, then the chemical reaction starts and a detonation wave is generated. The formation of the shock from a smooth flow is captured

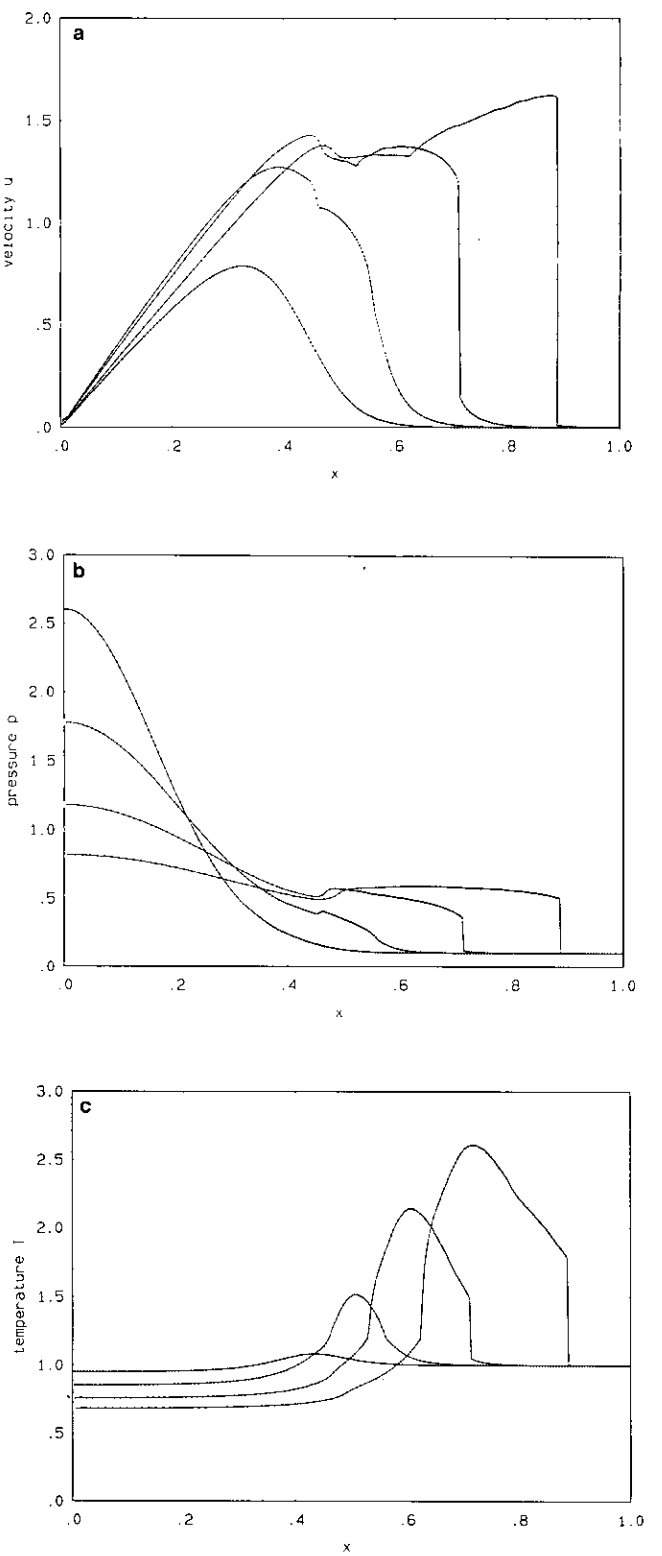


**FIG. 18.** (a) Velocity profiles for a smooth compression. (b) Pressure profiles for a smooth compression. (c) Temperature profiles for a smooth compression. When the compression raises the temperature above the critical value $T_c = 1.2$ the reaction begins and a detonation wave is formed; times $t = 0.075, 0.150, 0.225, 0.300$.

very well by this scheme. $N = 200$ computational cells were used. The numerical values used in this run are

$$\gamma = 1.4, \quad q_0 = 20, \; T_c = 1.2, \quad K = 1,$$

where all quantities are normalized appropriately. The normalization is such that the initial temperature of the gas at rest is $T_0 = 1$ or, equivalently, $\rho_0 = p_0$ in dimensionless units. The initial pressure distribution is given by

$$p_0(x) = 0.10 + 3.0 \exp(-25x^2).$$

## 5. CONCLUSIONS

An adaptive numerical scheme has been presented for the computation of flows with complicated interactions of discontinuous waves. Its accuracy and robustness, as demonstrated by numerical experiments make it a valuable tool, especially for the study of unsteady reacting flows with detonation waves. The conservative formulation gives the method all the advantages of higher-order shock-capturing schemes and its adaptive characteristic allows for good accuracy near shocks with no smearing effect. The advantages of the conservative shock-capturing schemes are combined with the advantages of the front-tracking methods very well to give a useful computational scheme.

The drawback is that the extension of this scheme to multidimensional flows is not straightforward. The main idea of the scheme is the conservative front-tracking of shocks and contact discontinuities on a Lagrangian grid. The Lagrangian aspect of the method is the most difficult to extend. The conservative front-tracking aspect can be extended and work in this area is in progress.

## ACKNOWLEDGMENTS

This work is part of a larger effort to investigate mixing and combustion, sponsored by the Air Force Office of Scientific Research Grant Nos. 88-0155 and 90-0304, whose support is gratefully acknowledged. The comments and suggestions of the referees are also greatly appreciated.

## REFERENCES

1. M. Ben-Artzi, *J. Comput. Phys.* **81**, 70 (1989).
2. M. J. Berger and J. Oliger, *J. Comput. Phys.* **53**, 484 (1984).
3. P. Colella and P. R. Woodward, *J. Comput. Phys.* **54**, 174 (1984).
4. W. Fickett and W. C. Davis, *Detonation* (Univ. of California Press, Berkeley, 1979).
5. S. K. Godunov, *Mar. Sb.* **47**, 271 (1959).
6. A. Harten, *J. Comput. Phys.* **49**, 357 (1983).
7. A. Harten, *SIAM J. Numer. Anal.* **21**, 1 (1984).
8. P. D. Lax and B. Wendroff, *Commun. Pure Appl. Math.* **13**, 217 (1960).
9. H. I. Lee and D. S. Stewart, *J. Fluid Mech.* **216**, 103 (1990).
10. R. W. McCormack, AIAA Paper No. 69-354 (unpublished).
11. J.-L. Montagné, H. C. Yee, and M. Vinokur, *AIAA J.* **27** (10), 1332 (1989).
12. G. Moretti, *Annu. Rev. Fluid Mech.* **19**, 313 (1987).
13. G. A. Sod, *J. Comput. Phys.* **27**, 1 (1978).
14. J. L. Steger and R. F. Warming, *J. Comput. Phys.* **40**, 263 (1981).
15. B. van Leer, *J. Comput. Phys.* **32**, 101 (1979).
16. B. van Leer, in *Lecture Notes in Phys.*, Vol. 170 (Springer-Verlag, New York/Berlin, 1982), p. 507.
17. B. van Leer, *SIAM J. Sci. Stat. Comput.* **5**(1), 1 (1984).
18. P. R. Woodward and P. Colella, *J. Comput. Phys.* **54**, 115 (1984).